Geophys. J. Int. (2000) **142,** 000–000

A Sea Level Equation for seismic perturbations

D. Melini[1], G. Spada[2] and A. Piersanti[1]

[1]*Istituto Nazionale di Geofisica e Vulcanologia, Sezione di Sismologia e Tettonofisica, Roma, Italy.*

[2]*Istituto di Fisica, Università degli Studi di Urbino "Carlo Bo", Urbino, Italy.*

SUMMARY

Large earthquakes are a potentially important source of relative sea level variations, since they can drive global deformation and simultaneously perturb the gravity field of the Earth. For the first time, we formalize a gravitationally self–consistent, integral sea level equation suitable for earthquakes, in which we account both for direct effects by the seismic dislocation and for the feedback from water loading associated with sea level changes. Our approach builds upon the well established theory first proposed in the realm of glacio–isostatic adjustment modeling. The seismic sea level equation is numerically implemented to model sea level signals following the 2004 Sumatra–Andaman earthquake, showing that surface loading from ocean water redistribution (so far ignored in post–seismic deformation modeling) may account for a significant fraction of the total computed post–seismic sea level variation.

Key words: Sea–level change, Sea Level Equation, Seismic deformation.

1 INTRODUCTION

The problem of future climate changes and their impact on human activities is still far from a complete solution (IPCC 2007). Nevertheless, the computational efforts devoted to this problem have reached a phase in which second–order complexities are often taken into account to achieve real world resolution levels (Shukla et al. 2006; Mitrovica et al. 2009; Bamber et al. 2009). The sea level variation associated with seismic activity is a representative of these second–order effects. In fact, long term

sea level change is driven primarily by eustatic processes, glacio–isostatic adjustments and thermo–compositional volume variations (IPCC 2007), while seismo–tectonic deformations play a small (but non negligible) role (Melini et al. 2004; Melini & Piersanti 2006).

The main shortcoming of the investigations so far is that, instead of approaching the full Sea Level Equation (hereinafter SLE), an approximated solution was computed only taking into account the direct effects of seismic sources on deformation and gravity potential variations (e.g. Melini & Piersanti 2006). This is justified in regional post–seismic investigations on time–scales of a few decades for which the isostatic response is expected to be negligible, but it is likely to be incorrect in global studies, where self–gravitation of the oceans plays a fundamental role (Farrell & Clark 1976). Recently, De Linage et al. (2009) solved a zeroth–order sea level equation for the short-term relaxation following the 2004 Sumatra-Andaman earthquake; according to their results, the response of the ocean has to be taken into account in order to correctly interpret the observed geoid perturbations. To improve these aspects of post–seismic rebound modeling, in this short note we describe and numerically solve a gravitationally self–consistent SLE for seismic perturbations, generalizing the results of Farrell and Clark (1976). In our study, the post–seismic deformation and gravity potential variation are first obtained by a semi–analytical, self–gravitating viscoelastic model (Piersanti et al. 1995), and are then used as initial conditions for an iterative solution scheme for the SLE, in which the loading problem associated with the mass redistribution of the oceans is solved using a post–glacial rebound calculator (Spada et al. 2004).

In Section 2 we discuss the theoretical aspects of our method and in Section 3 we focus on the details of numerical implementation, investigating the convergence of the iterative solution and addressing a simple synthetic problem. In Section 4 the method is used to evaluate the global and regional sea level variations following the Sumatra–Andaman earthquake of December 26, 2004.

2 METHODS

According to the theory of Farrell and Clark (1976), in the framework of glacio–isostatic adjustment (GIA) the SLE reads

$$S(\omega,t)=\left(\frac{\Phi}{\gamma}-U\right)+S^E-\overline{\left(\frac{\Phi}{\gamma}-U\right)}, \tag{1}$$

where S is sea level change, $\omega=(\theta,\lambda)$ denotes colatitude and longitude, t is time, Φ is the incremental gravity potential, γ is the reference gravity acceleration at the Earth surface, U is vertical displacement, and S^E is the eustatic sea level change, which represents the solution of the SLE in the case of a rigid, non–self–gravitating Earth:

$$S^E = -\frac{m_i}{\rho_w A_o}, \tag{2}$$

where m_i is the mass variation of ice sheets, ρ_w is the density of water, $A_o = \int_{oceans} dA$ denotes the (constant) area of the ocean surface and the overline indicates the average

$$\overline{(\dots)} = \frac{1}{A_o}\int_{oceans}(\dots)dA. \tag{3}$$

A SLE suitable for seismic perturbations can be readily obtained from Eq. (1) dropping the S^E term, since earthquakes do not imply any mass exchange with the oceans. However, the averaged term must be kept, since it ensures that the free surface of the oceans always coincides with the geoid (Farrell & Clark 1976). This gives:

$$S(\omega,t) = \left(\frac{\Phi}{\gamma} - U\right) - \overline{\left(\frac{\Phi}{\gamma} - U\right)}, \tag{4}$$

where $S(\omega,t)$ defines the history of sea level change at any point $\omega = (\theta,\lambda)$ on the sphere, and where now Φ and U are the total gravity potential variation and surface displacement imposed by the seismic dislocation, respectively. Consistently with the principle of mass conservation, in the seismic SLE (4), $\overline{S} = 0$.

The terms U and Φ in Eq. (4) stem from the sum of two contributions. The first, labeled by *eq* below, represents the direct effect of the seismic dislocation, while the second (*load*) is associated with the water load exerted by the changing sea level. Such decomposition is similar to that adopted in the framework of GIA studies (Spada & Stocchi 2006). Thus we write:

$$U(\omega,t) = U_{eq} + U_{load}(S) \tag{5}$$

and

$$\Phi(\omega,t) = \Phi_{eq} + \Phi_{load}(S), \tag{6}$$

where the S–dependence of the load terms can be expressed by a time–convolution between the viscoelastic loading–deformation coefficients $h_l(t)$ and $k_l(t)$ and the history of sea level change, which makes Eq. (4) an integral (implicit) equation. The lack of the eustatic term and the simple Heaviside time–history usually employed to describe the source (e.g. Piersanti et al. 1995) makes the seismic SLE formally simpler but does not alleviate the numerical complexity of the problem, as will be discussed below. In previous studies (Melini et al. 2004; Melini & Piersanti 2006), the ocean–averaged term in Eq. (4) was neglected. For an incompressible Earth, this is equivalent to the assumption of a uniform, non–self–gravitating ocean. Furthermore, the approximation $\Phi_{load} = U_{load} = 0$ was adopted, which reduces the SLE to

$$S(\omega,t) = \frac{\Phi_{eq}}{\gamma} - U_{eq}, \tag{7}$$

a fully explicit equation that can be solved as soon as the direct effect of earthquakes is determined.

A zeroth–order approximation to the solution S of the SLE (4) can be obtained neglecting Φ_{load} and U_{load} in front of the *eq* terms. With $\Phi_{eq} \equiv \Phi^{(0)}$ and $U_{eq} = U^{(0)}$, this gives:

$$S^{(0)}(\omega, t) = \left(\frac{\Phi^{(0)}}{\gamma} - U^{(0)}\right) - \overline{\left(\frac{\Phi^{(0)}}{\gamma} - U^{(0)}\right)}, \tag{8}$$

which is used to provide a first guess of the water load (mass per unit area) according to

$$L^{(0)}(\omega, t) = \rho_w S^{(0)} \mathcal{O}, \tag{9}$$

where $\mathcal{O}$ is the "ocean function" ($\mathcal{O} = 1$ over the oceans, and $\mathcal{O} = 0$ elsewhere) and where positive and negative values of L correspond to a sea level rise and fall, respectively. Once $L^{(0)}$ is determined globally, the response to loading U_{load} and Φ_{load} can be computed using pertinent load–deformation coefficients, providing a new estimate of the total displacement and gravity potential:

$$U^{(1)}(\omega, t) = U_{eq} + U_{load}(S^{(0)}) \tag{10}$$

$$\Phi^{(1)}(\omega, t) = \Phi_{eq} + \Phi_{load}(S^{(0)}), \tag{11}$$

which substituted into the right–hand side of Eq. (4) gives the new estimate of sea level change, $S^{(1)}$.

The method outlined above suggests the following general algorithm: *i)* given $S^{(k)}$, the k–th order approximation of the sea level change ($k = 0, 1, \ldots$), compute the water load function $L^{(k)}(\omega, t) = \rho_w S^{(k)} \mathcal{O}$ by Eq. (9), *ii)* using the direct responses to seismic dislocation and the solution to the loading problem, evaluate $U^{(k+1)} = U_{eq} + U_{load}(S^{(k)})$ and $\Phi^{(k+1)} = \Phi_{eq} + \Phi_{load}(S^{(k)})$, *iii)* from the SLE (4), compute the further approximation to sea level change $S^{(k+1)}$, *iv)* iterate until a previously defined convergence criterion is satisfied, *v)* if needed, provide final estimates for the total perturbation to gravity potential and vertical displacement field. This scheme is largely similar to that employed in GIA investigations, which has been thoroughly validated in a number of case–studies (see Spada & Stocchi (2006) and references therein), generally showing a fast convergence.

3 NUMERICAL IMPLEMENTATION

In our implementation, the response functions U_{eq} and Φ_{eq} in Eqs (5) and (6) are computed by the viscoelastic normal–mode approach originally proposed by Piersanti et al. (1995), for an incompressible, spherical self–gravitating model with Maxwell rheology. The algorithm outlined in Section 2 could be also applied to finely layered Earth models, possibly characterized by a generalized (linear) rheology (Spada & Boschi 2006; Spada 2008; Melini et al. 2008) or mantle compressibility (Pollitz 1997; Pollitz 2003). The response of the Earth to surface loading is evaluated by suitably adapting the TABOO post–glacial rebound calculator (Spada et al. (2004), see *http://samizdat.mines.edu/taboo/*). The model, described in Table 1, is characterized by a coarse 4–layer structure with PREM–averaged

density and rigidity and includes a low–viscosity upper mantle beneath a perfectly elastic lithosphere, and an homogeneous inviscid core. Considering the limitation of the post–seismic model by Piersanti et al. (1995) to 4 layers, the choice of upper mantle viscosity finds it motivation in the importance of the low–viscosity zone in the post–seismic relaxation process (Nostro et al. 1999; Piersanti et al. 2001).

The computation of surface integrals in Eq. (4) and of the responses to water load (i. e., functions U_{load} and Φ_{load} in Eqs (5) and (6) are practically performed with the aid of the icosahedron–based pixelization shown in Fig. 1, proposed by Tegmark (1996) for astrophysical applications. In the GIA context, this grid has been employed for the first time by Spada & Stocchi (2007) for solving numerically the SLE. The Tegmark discretization provides a natural set of Gauss points on the surface of the sphere and allows for a straightforward computation of surface integrals involving spherical harmonic (hereafter SH) functions as equal–weight finite sums. This property can be employed to compute ocean–averages as:

$$\overline{f} \simeq \mathcal{O}_{00}^{-1} \frac{1}{N} \sum_{i=1}^{N_w} f(\omega_i), \tag{12}$$

where f is a scalar function, N is the total number of pixels (according to Tegmark (1996), $N = 40R(R-1)+12$ where R is a resolution parameter), N_w is the number of ocean pixels, ω_i are their coordinates, and $\mathcal{O}_{00} \simeq 0.71$ is the degree zero and order zero harmonic coefficient of the ocean function (4π–normalized complex SH will be used throughout). For a given grid resolution R, Tegmark (1996) has shown that approximation (12) is numerically valid as long as the maximum degree of the SH expansion of f is $l_{max} \leq \sqrt{3N}$.

The icosahedron–based pixelization is also employed to discretize the surface load defined by Eq. (9). The load is distributed over axis–symmetrical disc–shaped elements with centers defined by the ocean pixels of Fig. 1, each with a diameter $d = 2a \arccos(1 - \frac{2}{N})$, a being Earth radius. Since resolving each load component requires an SH expansion to a degree $l_{max} \simeq 2\pi a/d$, a correct numerical implementation of the SLE thus requires

$$\frac{\pi}{\arccos\left(1 - \frac{2}{N}\right)} \leq l_{max} \leq \sqrt{3N} \tag{13}$$

that allows an optimal trade–off between grid spacing and computational costs to be determined. To satisfy Eq. (13), in our simulations we have used a grid with $N = 15212$ (this corresponds to $R = 20$) and considered harmonic degrees up to $l_{max} = 200$. The computation of U_{load} and Φ_{load} takes advantage of the symmetry of the load components, which makes these terms only dependent upon the colatitude of the observer relative to each elementary disc. The convolution integrals that involve load–deformation coefficients $h_l(t)$ and $k_l(t)$ and the history of sea level change within each

disk load are discretized in the time domain and computed by standard numerical methods (Spada et al. 2004).

To test the stability and the convergence of the solution scheme and to verify the absence of aliasing effects due to pixelization, we have performed a test imposing *ad–hoc* seismic effects. In particular, we set $\Phi_{eq} = 0$ and prescribe, for time $t \geq 0$, a vertical displacement $U_{eq} = -1$ m across a circular region of half–amplitude $\alpha = 5^\circ$ placed at $\omega = (\pi/2, \pi)$ (i. e., in the central Pacific Ocean). Thus, in this experiment,

$$S^{(k)}(\omega, t) = S^{(k)}_{load} - (U_{eq} - \overline{U_{eq}}) \approx S^{(k)}_{load} - U_{eq} \tag{14}$$

where $\overline{U_{eq}}$ is negligible in front of U_{eq} because of the localized displacement assumed for our toy earthquake, and using Eq. (4) the load–induced sea level variation is

$$S^{(k)}_{load}(\omega, t) = \left(\frac{\Phi_{load}(S^{(k)})}{\gamma} - U_{load}(S^{(k)}) \right) - \overline{\left(\frac{\Phi_{load}(S^{(k)})}{\gamma} - U_{load}(S^{(k)}) \right)}. \tag{15}$$

In Fig. 2, $S^{(k)}_{load}$ is shown for $k = 1, 2, 5$ and 10, as a function of time and for various source–observer angular distances Δ. For $\Delta = 0^\circ$ and relatively short times, $S^{(k)}_{load}$ slightly enhances the direct seismic effect $S^{(k)}_{eq} \equiv -U_{eq}$. However, with increasing time, $S^{(k)}_{load}$ becomes a large fraction ($\sim 40\%$) of the direct effect in the vicinity of the seismically deformed region, due to the visco–elastic relaxation induced by the water load. $S^{(k)}_{load}$ is large in the vicinity of the source and decays quickly with the observer distance, falling by a factor of $\sim 10^2$ moving from $\Delta = 0$ (frame a) to $\Delta = 20^\circ$ (c). It is interesting to observe that, in spite of the low–viscosity upper mantle (see Table 1), the $S^{(k)}_{load}$ curves are still far from equilibrium at time $t = 1$ kyrs after loading, a time–scale that largely exceeds the Maxwell relaxation time for this layer (3.7 yr). This may be interpreted as an effect of the response of the lower mantle, which is involved due to the relatively large size of the area of the "fault plane" employed in this synthetic case study. The density jump imposed at the depth of 670 km is also likely to play a role, due to the long relaxation times that characterize the return of compositional boundaries to equilibrium (Piersanti et al. 1995).

The issue of the convergence of the iterative scheme is addressed more quantitatively in Fig. 3, where the ratio $S^{(k)}_{load}/S^{(10)}_{load}$ is shown as a function of k for $\Delta = 0$ (a) and $\Delta = 20^\circ$ (b), and various times following the synthetic earthquake already considered in the previous figure. It is apparent that the convergence is monotonic ans relatively fast: these features are qualitatively similar to those observed when the SLE is solved for glacial forcing (e.g. Spada & Stocchi 2007). The spherically–averaged relative difference between subsequent iterations, defined as:

$$\epsilon^{(k)}_r(t) = \frac{1}{N} \sum_{i=1}^{N} \left| \frac{S^{(k)}(\omega_i, t) - S^{(k-1)}(\omega_i, t)}{S^{(k-1)}(\omega_i, t)} \right| \tag{16}$$

and shown in Fig. 4 for various values of time t, indicates that $k = 5$ ensures incremental errors well below the 0.1% threshold, which is fully acceptable for any practical implementation.

4 SEA LEVEL VARIATIONS FOLLOWING THE 2004 SUMATRA–ANDAMAN EARTHQUAKE

In this section we present an application of the proposed method to the sea level variations following the 2004 Sumatra–Andaman earthquake. The seismic source has been modeled with five point dislocations corresponding to the multiple CMT solution obtained by Tsai et al. (2005). These sources are obtained by fitting with the CMT method the long–period seismograms from the IRIS Global Seismographic Network. They account for a cumulative energy release corresponding to $M_w = 9.3$; their location and focal mechanisms are shown in Fig. 5. Using the semi–analytical model of global postseismic rebound originally developed by Piersanti et al. (1995) and subsequently extended by Soldati et al. (1998) and Boschi et al. (2000), we have obtained the time–dependent deformation and incremental gravitational potential U_{eq} and Φ_{eq}. These fields have been used as starting conditions to iteratively solve Eq. (4), as discussed in Section 2.

To evaluate the zeroth–order solution of the SLE defined in Eq. (8), we need to compute oceanic averages of U_{eq} and Φ_{eq} according to Eq. (3). Since the body–force equivalent representation of a point source is based on localized Dirac delta functions and their spatial derivatives (Smylie & Mansinha 1971; Mansinha et al. 1979), the spectra of U_{eq} and Φ_{eq} are rich at short wavelengths and decay slowly with harmonic degree (Casarotti 2003; Melini et al. 2008). For this reason, to obtain convergence, the SH expansion of the relevant scalar fields (U_{eq} and Φ_{eq}) has to be truncated to $l_{max} \approx 10^3 - 10^4$, depending on the source–observer distance (Sun & Okubo 1993; Riva & Vermeersen 2002; Casarotti 2003). In the present application, the postseismic solutions reach a stable convergence for $l_{max} = 4000$. Since for numerical stability of Eq. (3) the relation $l_{max} \leq \sqrt{3N}$ must be satisfied, the computation of $\overline{U_{eq}}$ and $\overline{\Phi_{eq}}$ requires a pixelization with $N \geq 5.3 \times 10^6$ points, corresponding to a resolution $R = 366$. We remark that, due to the linearity of oceanic integrals, this high–resolution pixelization is not needed in subsequent iterations of the SLE solution scheme. Indeed, once $\overline{U_{eq}}$ and $\overline{\Phi_{eq}}$ are known, the evaluation of oceanic integrals of Eqs (5) and (6) requires only the integration of *load* terms, which can safely be carried out with an $R = 20$ pixelization, as discussed in the previous section. The computation of $\overline{U_{eq}}$ and $\overline{\Phi_{eq}}$ on the high–resolution grid represents a very intensive numerical task: even with a highly optimized parallel integration code on a 128–core distributed–memory cluster, it requires about 15 hours for each point source. For this reason, while a 2D source modeling would be certainly more realistic (Nostro et al. 1999), we are currently limited to the point–source approximation; indeed, considering the exceptionally large rupture extension of the

Sumatra earthquake, modeling a 2D source through a superposition of point sources would increase the computation time above acceptable levels, even adopting a relatively coarse source discretization. We remark that the iterative solution method for the SLE which has been outlined in Section 2 is independent from the postseismic deformation model, which is used only to provide initial conditions to the iterative solution scheme. The seismic SLE can therefore be solved with the same prescriptions if a more detailed model of postseismic deformation is employed. For the present application, whose aim is a demonstration of the water load effects in a real case, we will theredore use a point source approximation which anyway gives acceptable results on a global scale.

In Fig. 6 the average relative difference between iterations $\epsilon_r^{(k)}(t)$, as defined by Eq. (16), is shown for a range of observation times. From a comparison with Fig. 4 it can be observed that, when a real seismic source is employed, the convergence of the iteration scheme is less regular than in the synthetic case. This is likely to be the result of the increased numerical noise introduced by the rich spectrum of harmonics that characterize the realistic seismic source compared with the 'hat' test displacement considered in Section 3. In spite of this, however, after $k = 4$ iterations the average relative difference is $\leq 5\%$ and for $k = 10$ it is below the 1% level. Looking at the spatial patterns of $S^{(k)}(\omega, t)$, we have verified that less regular convergence specifically results from contributions to $\epsilon_r^{(k)}(t)$ from regions close to the nodal lines of this function, where some of the terms in Eq. (16) become numerically indeterminate, because of $S^{(k)} \simeq 0$, even if the solution has already reached a stable convergence in the bulk of the spatial domain.

In Figs 7 and 8 we quantitatively evaluate the effect of water load upon sea level changes, focussing on a global and a regional scale, respectively. The left frames show snapshots of $S^{(k=0)}(\omega, t)$, which only accounts for the effect of the seismic dislocation source, computed according to Eq. (8), while in the right frames we consider $S_{load} = S^{(k=10)} - S^{(k=0)}$. From Fig. 7, the term S_{load} turns out to be smaller than the seismic contribution, but definitely not negligible, being a significant fraction of the total signal even on a global scale. Its relative weight increases with time, due to the delayed viscoelastic response of the ductile layers to the forcing of the seismically–induced sea level variations. For the local scale analysis of Fig. 8, it results that the effect of the water load correction is even stronger, but the results may be affected to some degree by the point–source approximation which can affect significantly the near–field computations (Nostro et al. 1999). For short time–scales (a few years) the load correction is manifest as a broad sea level fall, with a smoothed pattern with respect to the negative lobe associated with the purely seismic contribution, consistently with the results of the synthetic case discussed above. For longer time–scales ($t = 100$ yrs in Fig. 8) the contribution to sea level from water load broadly follows the pattern of alternating lobes of the seismic term; this is

a common feature found in postseismic relaxation of low–dip thrust faults (Rundle 1982; Volpe et al. 2007).

Fig. 9 shows predictions of post–seismic sea level variations at ten tide–gauge sites belonging to the PSMSL network (see *http://www.pol.ac.uk/psmsl/*), whose locations are shown in Fig. 5. Solid and dashed curves show results obtained neglecting and including the water load in the SLE, respectively. All the sites share a qualitatively similar history of sea level variations, in which a post–seismic viscoelastic "wave" follows a quiescent initial phase on time–scales of a few centuries. As we have found with the synthetic tests of Fig. 2, this time–scale exceeds the intrinsic Maxwell characteristic time of mantle layers, suggesting that relaxation of internal compositional boundaries are indeed playing a role, due to the large extent of the seismic source (Piersanti et al. 1995). At near–field sites (e. g., Ko Taphao Noi), our computations predict a sea level fall of ~ 1 m during the next century, which would imply average rates of sea level change that greatly exceed the secular globally averaged trend, close to 1.5 mm/yr (IPCC 2007). Sensibly smaller (but still significant) effects are predicted for other sites (Kanmen, Manila, and Danang), with a sea level rise of up to ~ 5 cm during the same period. The average trend, in this case, is $\sim 30\%$ of the current average global trend, and practically negligible in comparison with the local sea level trend which amounts to ~ 12 mm/yr during the last few decades in the case of Manila (Spencer & Woodworth 1993). While corrected and un–corrected sea level predictions are generally similar on a decade time–scale, they may diverge for longer periods, when the water loading effect may perturb the seismic contribution significantly, by values ranging between 10 and 20%. This is also found for "far–field" tide–gauges (e. g., Port Louis and Broome), where numerical artifacts due to the point–source approximation are likely to have a minor role. In Fig. 10 the synthetic sea level time series are plotted on a 20–year period, during which they are well approximated by a linear trend. With a least–squares linear regression (see dotted lines), an estimate of the rate of sea level variation has been obtained from the results of Fig. 10; numerical values are listed in Table 2. The contribution to the rate of sea level variation due to the load correction, $\dot{S}_{load}$, turns out to be a large fraction the total trend, with a relative impact up to nearly 50% at Vishakhapatnam.

The coseismic and postseismic gravity field perturbations following the 2004 Sumatra earthquake have been evidenced by GRACE satellite measurements. Several authors have extracted the earthquake signature from the GRACE solutions and found it to be consistent with seismological models (Han et al. 2006; Ogawa & Heki 2007; Panet et al. 2007). Recently, De Linage et al. (2009) modeled the postseismic geoid perturbation taking into account the static potential perturbation of a global incompressible ocean; according to their results, the oceanic contribution is needed in order to successfully reproduce the spatial features of the postseismic geoid perturbation observed by GRACE. As we verified by extracting the geoid signal from our results, the oceanic term obtained by De Linage et al.

(2009) has the same sign and spatial extension of the short–term water load effect resulting from our simulations, even if the seismic source model employed by De Linage et al. (2009) is more realistic than our point–source approximation. Our simulations predict larger peak values of geoid perturbation, which is probably a bias effect of the point source model which leads to an overestimation of coseismic effects in the near–field (Piersanti et al. 1997).

The spectral features of the sea level correction due to ocean loading can be investigated by computing the harmonic coefficients

$$c_{lm}(t) = \int_{\Omega} \mathcal{Y}^{*}_{lm}(\omega) S_{load}(\omega, t) d\Omega, \tag{17}$$

where Ω is the unit sphere and $\mathcal{Y}_{lm}$ are the 4π–normalized complex SH. The normalized squared coefficients $|c_{lm}|^2 / \max_{l,m}\left(|c_{lm}|^2\right)$, displayed in the diagrams of Fig. 11, show that on time–scales of a few years most of the signal is confined to low harmonic degrees, while for longer times the relative weight of higher harmonics increases. This indicates the presence of short–wavelength features of the sea level signal in the area surrounding the seismic source as a consequence of stress concentration due to viscoelastic relaxation in the ductile layer, which for low–angle thrust faults may result in small–scale regions of opposite vertical deformation around the source location (Rundle 1982; Volpe et al. 2007).

5 CONCLUSIONS

For the first time we have obtained a solution for the gravitationally self–consistent SLE describing sea level perturbations occurring after a large earthquake. The SLE has been solved numerically by implementing an iterative scheme directly derived from those adopted in GIA studies (see e. g., Spada & Stocchi, 2006). As a result, our analysis shows that feedback loading effects play a significant role in assessing seismic quasi–static sea level variations. The viability of the proposed approach has been assessed by means of a synthetic test with a disc–shaped oceanic load in order to verify its numerical stability. The solution convergence turns out to be monotonic and relatively fast, similarly to what is observed in post–glacial rebound applications (Spada & Stocchi 2007).

The method has then been applied to the prediction of sea level variations following the 2004 Sumatra–Andaman earthquake. We found that loading effects represent an important contribution to seismically induced sea level variations on time–scales ranging from a few decades up to several thousands of years. These time–scales, which largely exceed the Maxwell relaxation times of the involved layers, suggest that relaxation modes connected to internal compositional boundaries are excited. An analysis of the predicted sea level signal on a set of PSMSL tide–gauge sites showed that, for “near–field” stations, the expected post–seismic effect is not negligible even in comparison with the

globally–averaged secular trend, although this result may be biased by the point–source approximation which is currently unavoidable due to computational requirements.

The presence of long–term effects suggests that a detailed knowledge of historical seismicity is crucial in modeling present–day sea level rates. For timescales of a few years, the sea level signal follows an approximately linear trend, and the loading term represents a non negligible perturbation to the total rate. These short–term effects may be further enhanced in the presence of rheological layers characterized by a transient rheology, since in that case a large postseismic signal occurs on time scales of the order of months (Pollitz 2003).

In this respect, we can conclude that a detailed modeling of sea level change cannot neglect the effect of seismic perturbations, which can be the predominant contribution in correspondence of subduction zones characterized by large seismic energy release. Future high–resolution scenarios of sea level variation should take into account, among other contributions, the highly heterogeneous signals coming from short wavelength regional seismic activity, in order to precisely assess the exact role played by different phenomena in determining sea level variation. The inclusion of seismic effects in a comprehensive approach based on a self–consistent solution of the SLE represents an opportunity to create a unified formal framework to model non–eustatic sea level variations.

ACKNOWLEDGMENTS

We thank John Beavan, Wenke Sun and Riccardo Riva for their careful and incisive reviews. This work is partly supported by MIUR (Ministero dell'Istruzione, dell'Università e della Ricerca) with the PRIN2006 grant "Il ruolo del riaggiustamento isostatico postglaciale nelle variazioni del livello marino globale e mediterraneo: nuovi vincoli geofisici, geologici ed archeologici" and the FIRB grant "Sviluppo di nuove tecnologie per la protezione e la difesa del territorio dai rischi naturali". The figures have been prepared with the GMT software by Wessel & Smith (1991).

REFERENCES

Bamber, J., Riva, R., Vermeersen, L.L.A. & Lebrocq, A., 2009. Reassessment of the potential sea–level rise from a collapse of the West Antarctic ice sheet, *Science*, **324**, 901–903.

Boschi, L., Piersanti, A. & Spada, G., 2001. Global post–seismic deformation: Deep earthquakes, *J. geophys. Res.*, **105** (1), 631–652.

Casarotti, E., 2003. *Postseismic stress diffusion in a spherical viscoelastic Earth model*, PhD Thesis, University of Bologna, Italy.

De Linage, C., Rivera, L., Hinderer, J., Boy, J.P., Rogister, Y., Lambotte, S. & Biancale, R., 2009. Separation of coseismic and postseismic gravity changes for the 2004 Sumatra–Andaman earthquake from 4.6 yr of

GRACE observations and modelling of the coseismic change by normal–modes summation, *Geophys. J. Int.*, **176** (3), 695–714.

Farrell, W. E. & Clark, J. A., 1976. On postglacial sea level. *Geophys. J. R. astr. Soc.*, **46**, 647–667.

Han, S., Shum, C., Bevis, M., Ji, C. & Kuo, C., 2006. Crustal dilatation observed by GRACE after the 2004 Sumatra-Andaman earthquake, *Science*, **313**, 658–662.

IPCC, 2007. *Climate Change 2007: The Physical Science Basis*, Cambridge Univ. Press, Cambridge.

Mansinha, L., Smylie, D.E. & Chapman, C.H., 1979. Seismic excitation of Chandler wobble revisited, *Geophys. J. R. astr. Soc.*, **59**, 1–17.

Melini, D., Piersanti, A., Spada, G., Soldati, G. & Casarotti, E., 2004. Earthquakes and relative sea level changes, *Geophys. Res. Lett.*, **31** (9), L09601.

Melini, D. & Piersanti, A., 2006. Impact of global seismicity on sea level change assessment, *J. geophys. Res.*, **111**, B03406.

Melini, D., Cannelli, V., Piersanti, A. & Spada, G., 2008. Post–seismic rebound of a spherical Earth: new insights from the application of the Post–Widder inversion formula, *Geophys. J. Int.*, **174**, 672–695, doi: 10.1111/j.1365-246X.2008.03847.x.

Mitrovica, J. X., Gomez, N. & Clark, U., 2009. The sea–level fingerprint of West Antarctic collapse, *Science*, **323**, 753.

Nostro, C., Piersanti, A., Antonioli, A. & Spada, G., 1999. Spherical versus flat models of coseismic and post-seismic deformations, *J. geophys. Res.*, **104** (B6), 13,115–13,134.

Ogawa, R. & Heki, K., 2007. Slow postseismic recovery of geoid depression formed by the 2004 Sumatra–Andaman Earthquake by mantle water diffusion, *Geophys. Res. Lett.*, **34** (6), L06313.

Panet, I., Mikhailov, V., Diament, M., Pollitz, F., King, G., De Viron, O., Holschneider, M., Biancale, R. & Lemoine, J., 2007. Coseismic and postseismic signatures of the Sumatra 2004 December and 2005 March earthquakes in GRACE satellite gravity, *Geophys. J. Int.*, **171** (1), 177–190.

Piersanti, A., Spada, G., Sabadini, R. & Bonafede, M., 1995. Global postseismic deformation, *Geophys. J. Int.*, **120** (3), 544–566.

Piersanti, A., Spada, G. & Sabadini, R., 1997. Global postseismic rebound of a viscoelastic earth: theory for finite faults and application to the 1964 Alaska earthquake, *J. geophys. Res.*, **102**, 477–492.

Piersanti, A., Nostro, C. & Riguzzi, F., 2001. Active displacement field in the Suez–Sinai area: the role of postseismic deformation. *Earth planet. Sci. Lett.*, **193**, 13–23.

Pollitz, F.F., 1997. Gravitational viscoelastic postseismic relaxation on a layered spherical earth, *J. geophys. Res.*, **102**, 17921–17941.

Pollitz, F.F., 2003. Transient rheology of the uppermost mantle beneath the Mojave Desert, California, *Earth planet. Sci. Lett.*, **215**, 98–104.

Riva, R. & Vermeersen, L., 2002. Approximation method for high–degree harmonics in normal mode modeling, *Geophys. J. Int.*, **151**, 309–313.

Rundle, J.B., 1982. Viscoelastic–gravitational deformation by a rectangular thrust fault in a layered Earth, *J.*

geophys. Res., **87** (B9), 7,787–7,796.

Shukla, J., Del Sole, T., Fennessy, M., Kinter, J. & Paolino, D., 2006. Climate Model Fidelity and Projections of Climate Change, *Geophys. Res. Lett.*, **33**, L07702, doi:10.1029/2005GL025579.

Smylie, D.E. & Mansinha, L., 1971. The elasticity theory of dislocations in real Earth models and changes in the rotation of the Earth, *Geophys. J. R. astr. Soc.*, **23**, 329–354.

Soldati, G., Piersanti A. & Boschi, E., 1998. Global postseismic gravity changes of a viscoelastic Earth, *J. geophys. Res.*, **103**, 29,867–29,885.

Spada, G., Antonioli, A., Boschi, L., Cianetti, S., Galvani, G., Giunchi, C., Perniola, B., Piana Agostinetti, N., Piersanti, A. & Stocchi, P., 2004. Modeling Earth's postglacial rebound, *EOS, Trans. Am. geophys. Un.*, **85**, 62–64.

Spada, G. & Stocchi, P., 2006. *The Sea Level Equation, Theory and Numerical Examples*, Aracne, Roma, ISBN: 88-548-0384-7.

Spada, G. & Boschi, L. 2006. Using the Post–Widder formula to compute the Earth's viscoelastic Love numbers, *Geophys. J. Int.*, **166** (1), 309–321, doi: 10.1111/j.1365-246X.2006.02995.x.

Spada, G. & Stocchi, P., 2007. SELEN: a Fortran 90 program for solving the "Sea Level Equation", *Comput. and Geosci.*, **33** (4), 538–562, doi: 10.1016/j.cageo.2006.08.006.

Spada, G., 2008. ALMA, a Fortran program for computing the visco–elastic Love numbers of a spherically symmetric planet, *Comput. and Geosci.*, **34** (6), 667–687, doi: 0.1016/j.cageo.2007.12.001.

Spencer, N. E. & Woodworth, P. L., 1993. *Data holdings of the Permanent Service for Mean Sea Level*, Permanent Service for Mean Sea Level, Bidston, Birkenhead, UK.

Sun, W. & Okubo, S., 1993. Surface potential and gravity changes due to internal dislocations in a spherical earth – I. Theory for a point dislocation, *Geophys. J. Int.*, **114** (3), 569–592.

Tegmark, M., 1996. An icosahedron–based method for pixeling the celestial sphere, *Astrophys. J.*, **470**, L81–L84.

Tsai, V. C., Nettles, M., Ekström, G. & Dziewonski, A. M., 2005. Multiple CMT source analysis of the 2004 Sumatra earthquake, *Geophys. Res. Lett.*, **32**, L17034.

Volpe, M., Melini D. & Piersanti, A., 2007. FEMSA: a finite element simulation tool for quasi–static seismic deformation modeling, *Ann. Geophys.*, **50** (3), 367–385.

Wessel, P., & Smith, W. H. F., 1991. Free software helps map and display data, *EOS, Trans. Am. geophys. Un.*, **72**, 441.

Yuen, D. A. & Peltier, W. R., 1982. Normal modes of the viscoelastic earth, *Geophys. J. R. astr. Soc.*, **69**, 495–526.

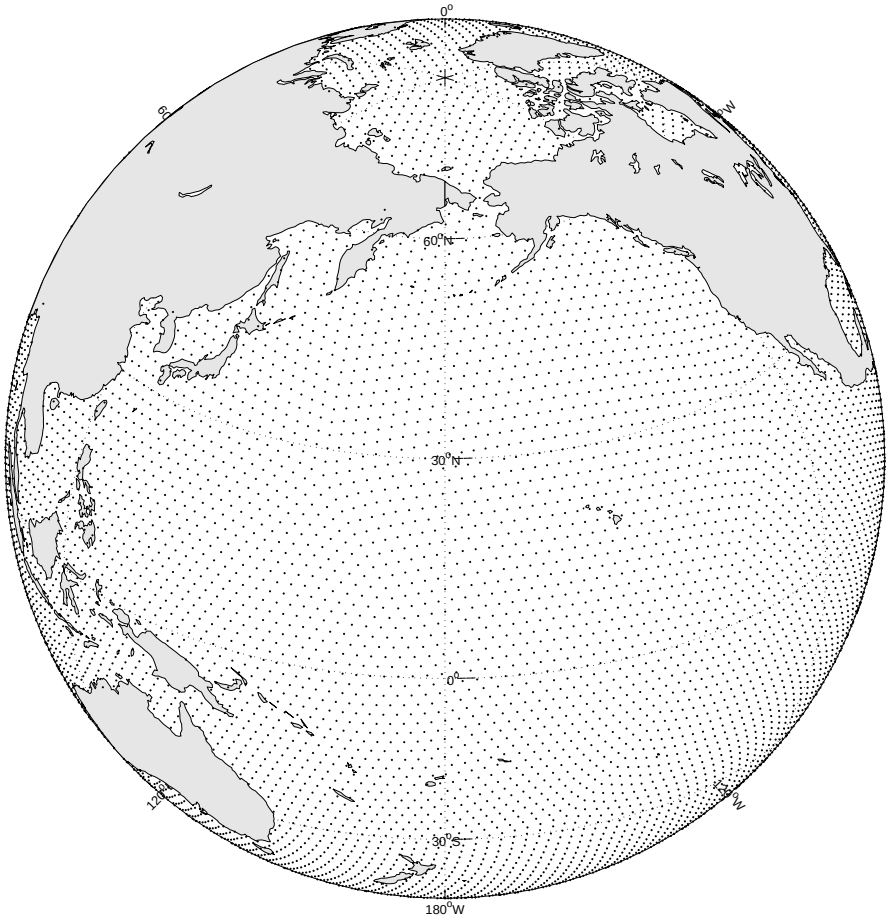

Figure 1. The Tegmark (1996) pixelization. The dots are the centroids of slightly distorted, equal–area hexagons. The code that generates the pixels coordinates is available from *http://space.mit.edu/home/tegmark/*. Wet and dry pixels are separated from the global distribution using the GMT utilities (Wessel & Smith 1991), freely downloadable from *http://gmt.soest.hawaii.edu/*.

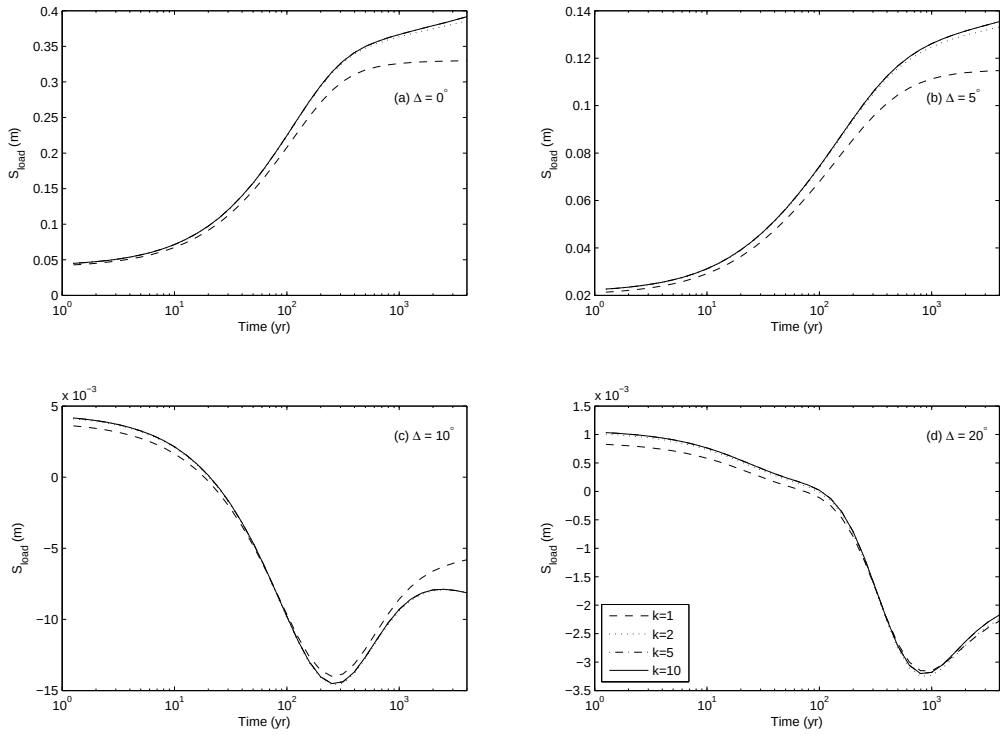

Figure 2. Temporal dependence of $S_{load}^{(k)}$ in the synthetic case for observer distances $\Delta = 0°$ to $20°$. Different curves show estimates for $k = 1, 2, 5$ and 10.

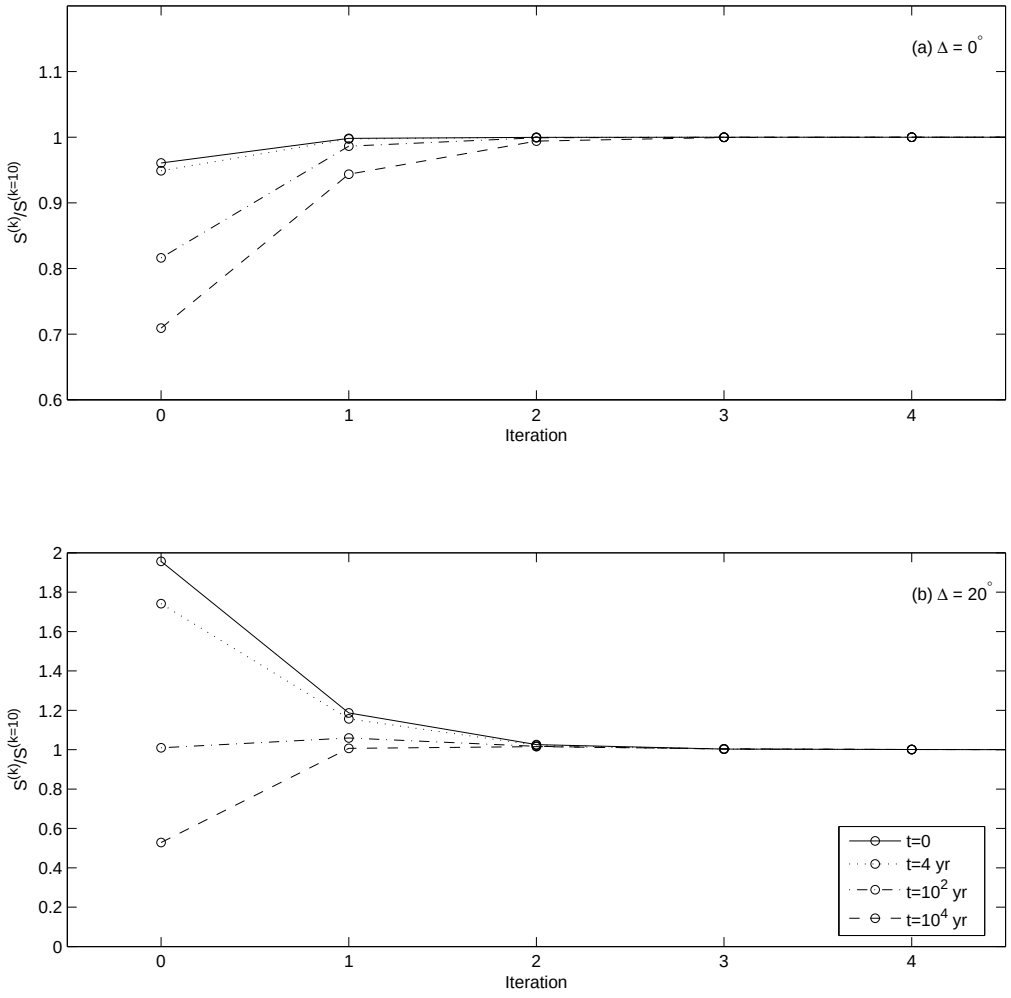

Figure 3. Dependence of $S^{(k)}_{load}/S^{(10)}_{load}$ upon the iteration k for observer distance $\Delta = 0$ and 20° in the synthetic case. Different lines represent observation times as shown in legend.

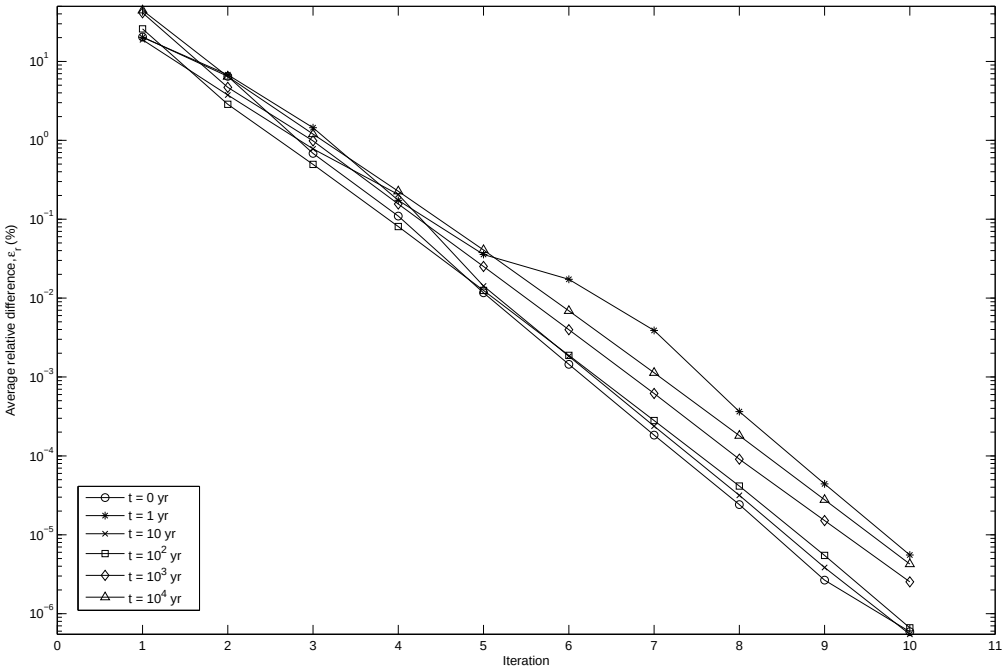

Figure 4. Average relative difference between iterations, $\epsilon^{(k)}$, for various k values. Different curves pertain to distinct observation times. See Eq. (16) for the definition of $\epsilon^{(k)}$.

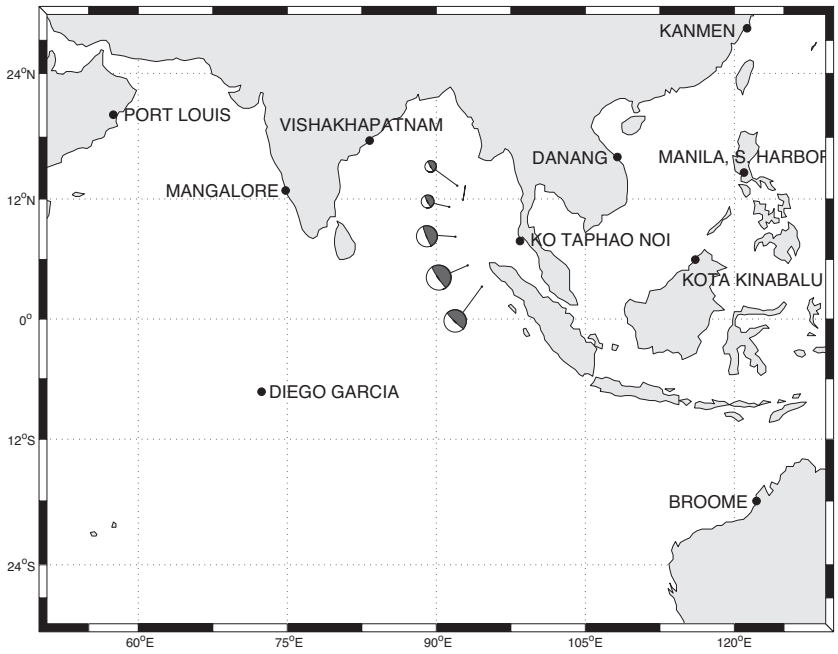

Figure 5. Focal mechanisms of the five point sources employed to simulate the rupture of the 2004 Sumatra–Andaman earthquake. The figure also shows the location of the ten PSMSL stations considered in this study (see Table 2).

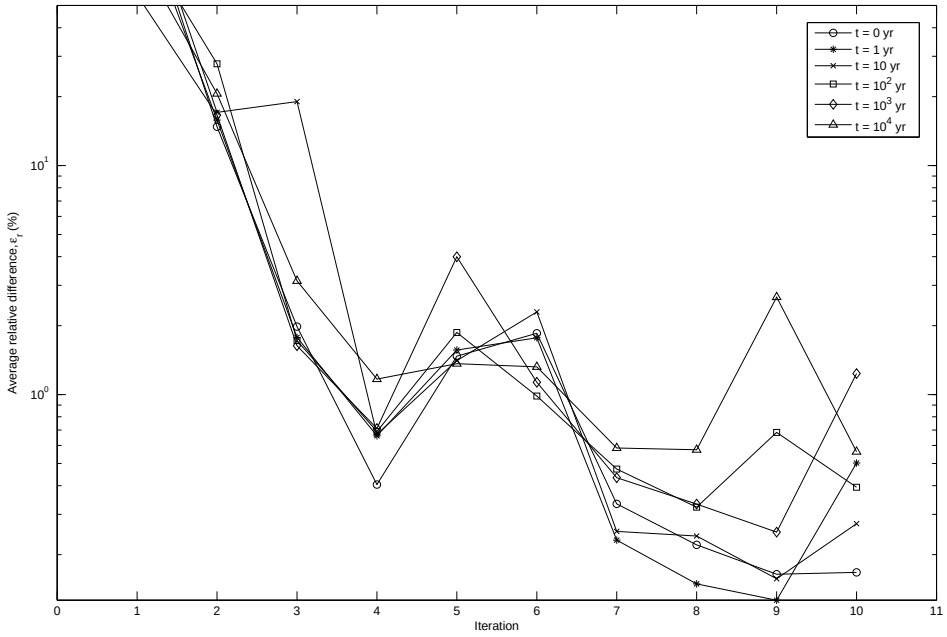

Figure 6. Average relative difference between iterations, $\epsilon^{(k)}$, in the case of the 2004 Sumatra–Andaman earthquake. See Eq. (16) for the definition of $\epsilon^{(k)}$.

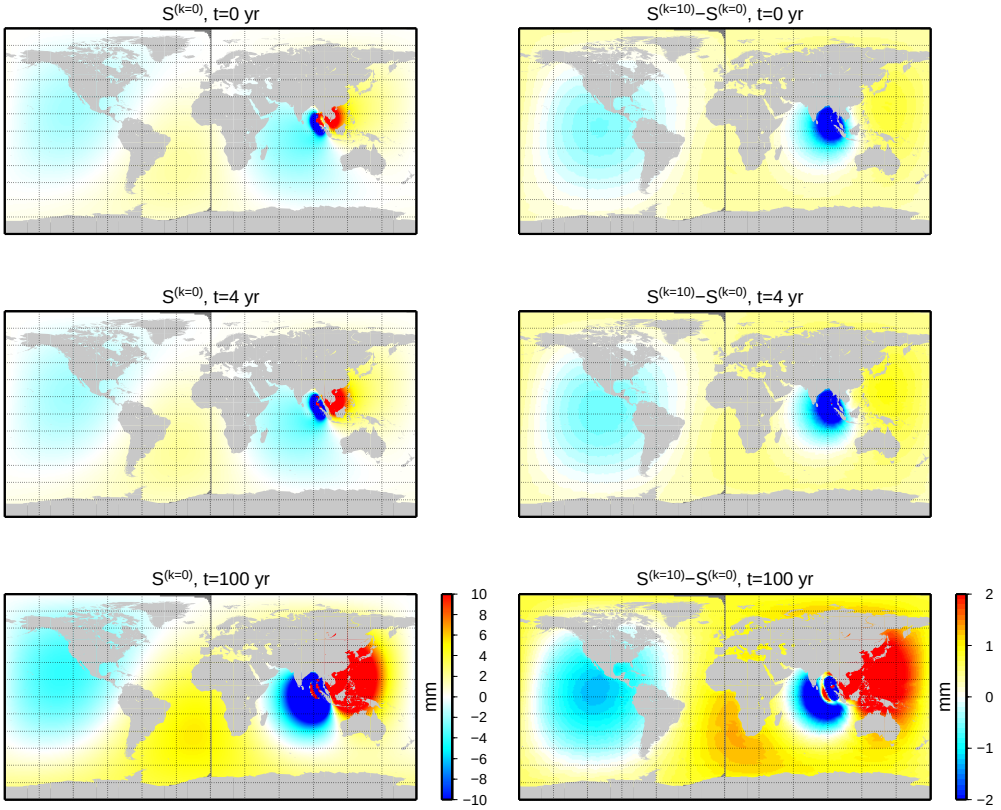

Figure 7. Global sea level change associated with the 2004 Sumatra–Andaman earthquake for various times after the main shock. Left frames only show the direct seismic contribution. The effect of the ocean loading term is shown in the right frames.

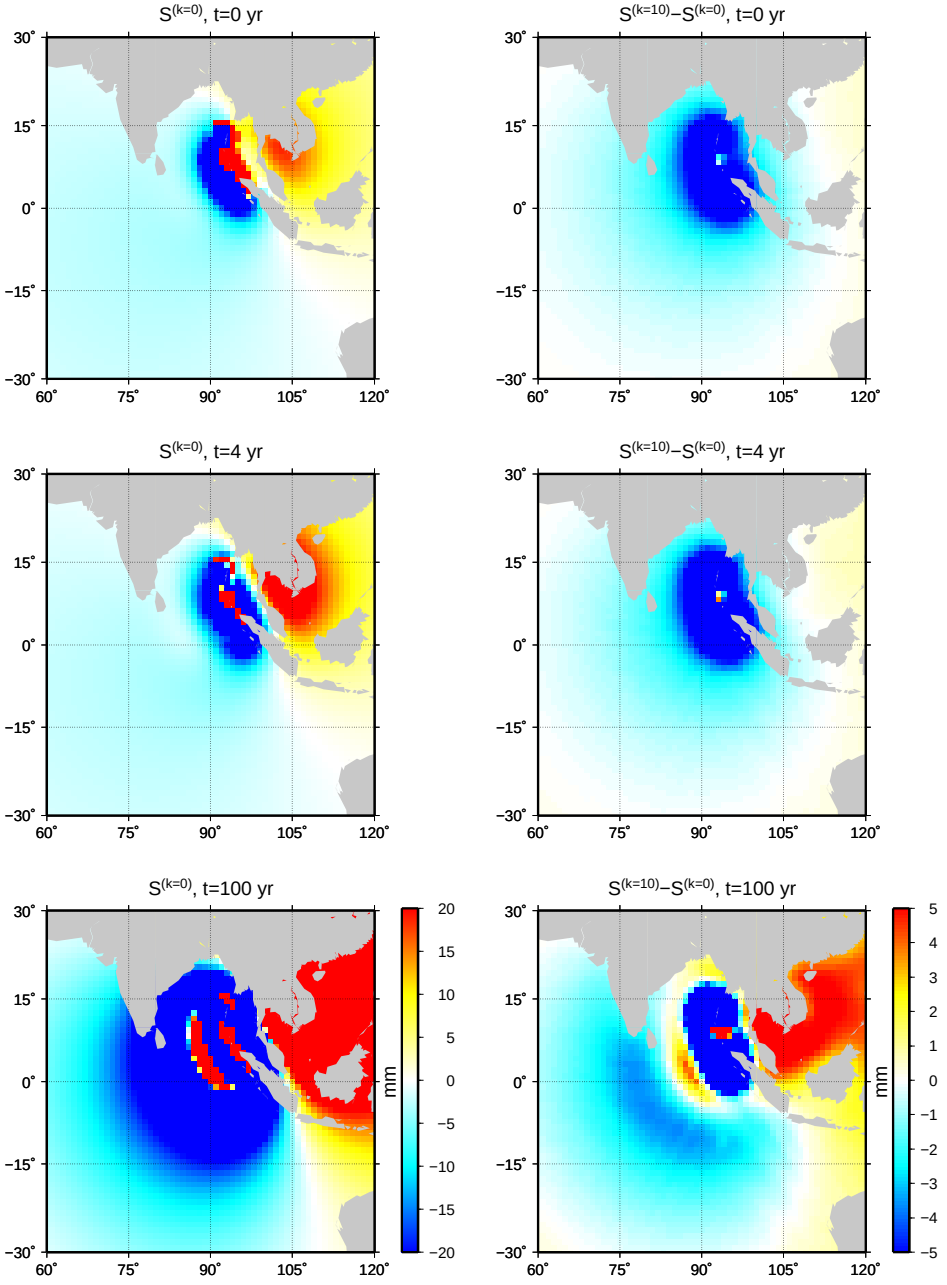

Figure 8. As in Fig. 7, but on a regional scale.

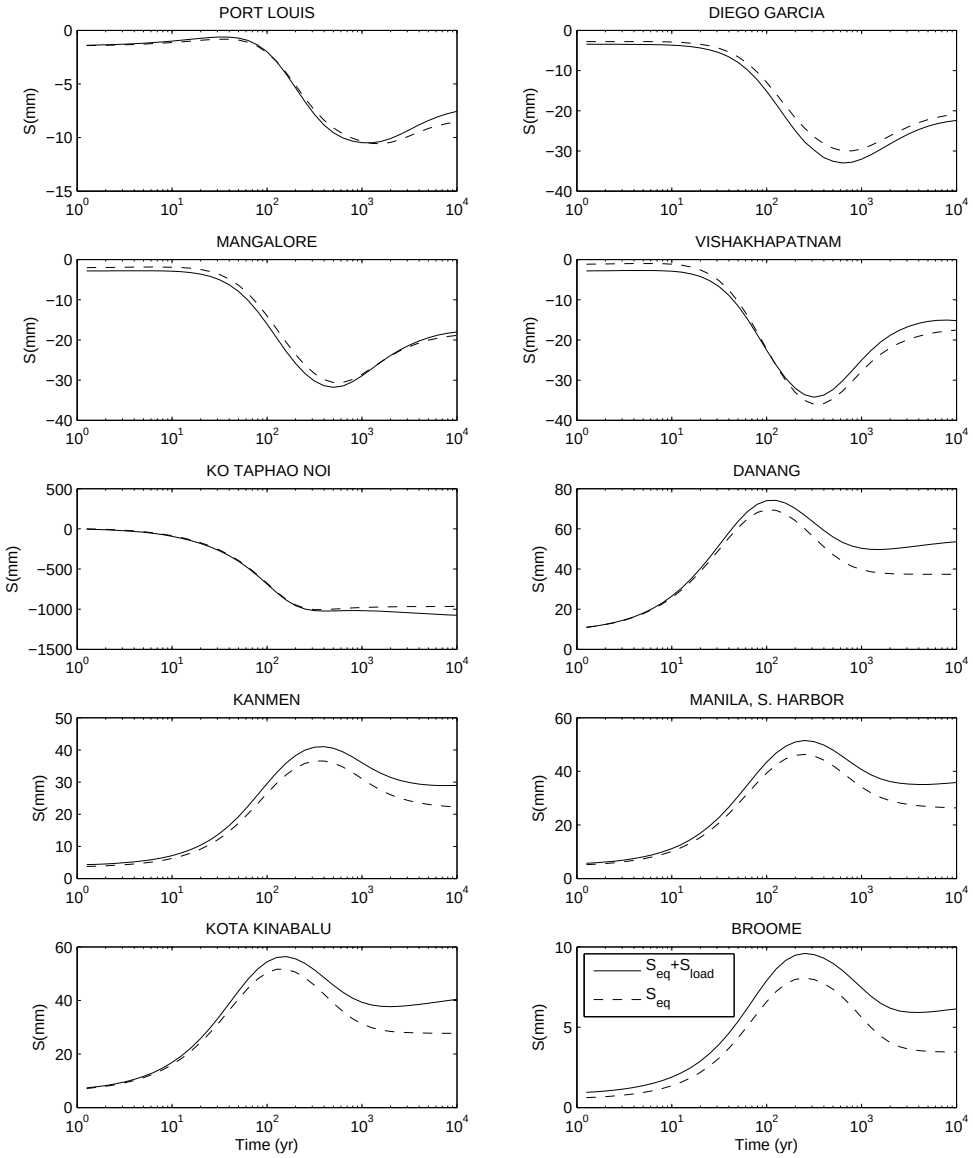

Figure 9. Sea level variations driven by the 2004 Sumatra–Andaman earthquake at the PSMSL sites whose location is shown in Fig. 5. Solid and dashed curves show results obtained using the seismic SLE with and without the ocean load included, respectively.

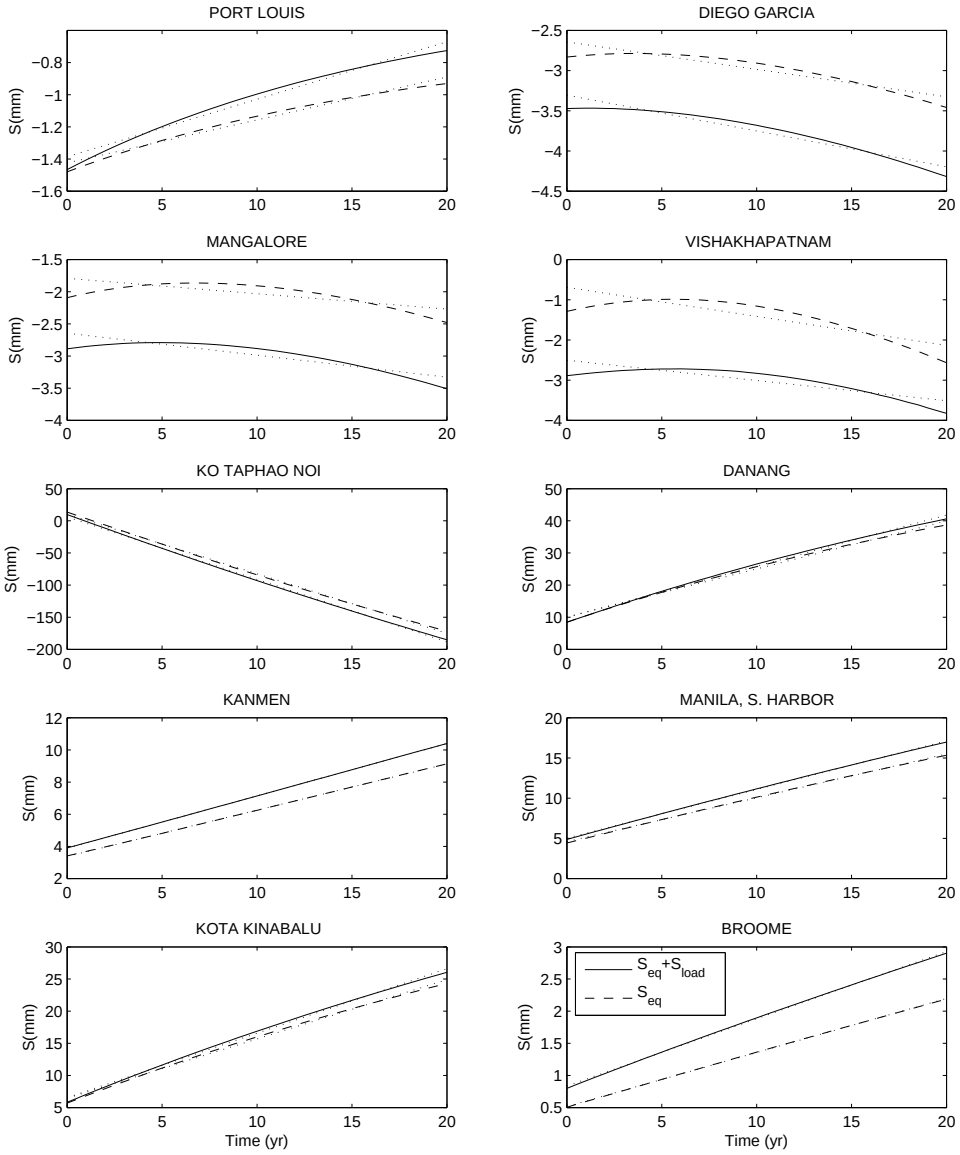

Figure 10. The same as in Fig. 9, but on a time period of 20 years following the main shock. Dotted lines show least–squares trends of the individual solutions.

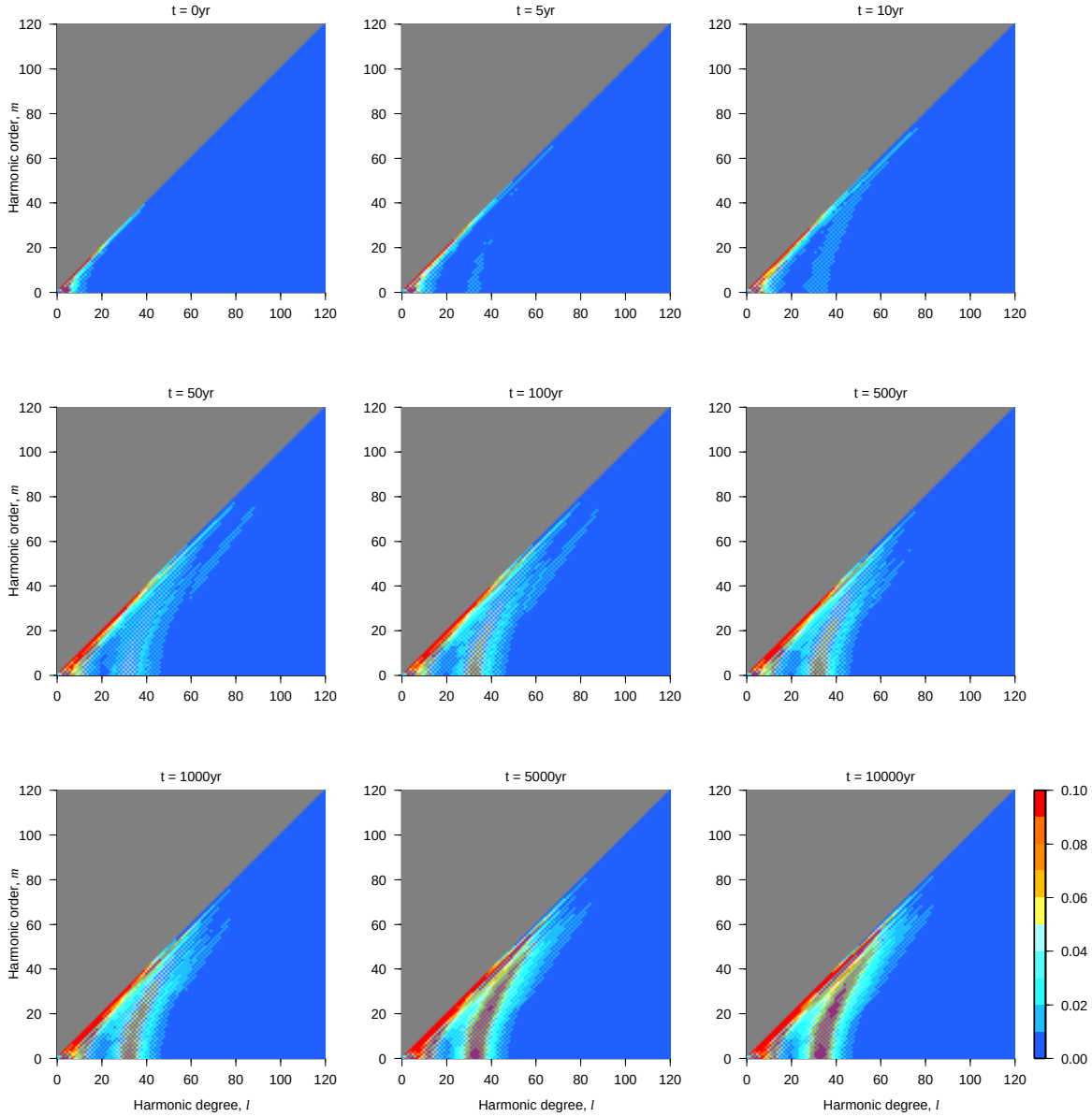

Figure 11. Non–dimensional, normalized spectral coefficients in the range of harmonic degrees $2 \leq l \leq 120$ computed according to Eq. (17).

Table 1. Model parameters employed in this study.

Layer	Radius, r (km)	Density, ρ (10^3 kg m^{-3})	Rigidity, μ (10^{10} Pa)	Viscosity, η (10^{21} Pa s)
1. Lithosphere	6291 – 6371	3.115	5.597	∞
2. Upper mantle	5701 – 6291	3.614	8.464	0.01
3. Lower mantle	3480 – 5701	4.878	21.710	1
4. Core	0 – 3480	10.932	0	0

Table 2. Observed and predicted rates of sea level change at the PSMSL sites considered in this study. PSMSL rates, obtained from *http://www.pol.ac.uk/psmsl/*, are computed by standard least–squares over the whole time period of observations. Modelled rates are obtained by linear interpolation of the synthetic S–curves shown in Fig. 9.

PSMSL station	Observed rate (mm/yr)	$\dot{S}$ (mm/yr)	$\dot{S}_{load}$ (mm/yr)
Port Louis	-0.94 ± 1.90	0.04	0.01
Diego Garcia	2.26 ± 3.63	-0.05	-0.01
Mangalore	-1.08 ± 1.39	-0.03	-0.01
Vishakhapatnam	0.72 ± 0.31	-0.05	0.02
Ko Taphao Noi	0.08 ± 0.62	-9.72	-0.46
Danang	2.50 ± 0.92	1.59	0.10
Kanmen	1.70 ± 0.32	0.33	0.04
Manila, S. Harbor	6.68 ± 0.43	0.61	0.06
Kota Kinabalu	3.78 ± 2.21	1.00	0.08
Broome	11.64 ± 4.52	0.11	0.02